

ORIGINAL ARTICLE

Tracer kinetic modeling of [^{11}C]AFM, a new PET imaging agent for the serotonin transporterMika Naganawa¹, Nabeel Nabulsi¹, Beata Planeta¹, Jean-Dominique Gallezot¹, Shu-Fei Lin¹, Soheila Najafzadeh¹, Wendol Williams¹, Jim Ropchan¹, David Labaree¹, Alexander Neumeister², Yiyun Huang¹ and Richard E Carson¹

[^{11}C]AFM, or [^{11}C]2-[2-(dimethylaminomethyl)phenylthio]-5-fluoromethylphenylamine, is a new positron emission tomography (PET) radioligand with high affinity and selectivity for the serotonin transporter (SERT). The purpose of this study was to determine the most appropriate kinetic model to quantify [^{11}C]AFM binding in the healthy human brain. Positron emission tomography data and arterial input functions were acquired from 10 subjects. Compartmental modeling and the multilinear analysis-1(MA1) method were tested using the arterial input functions. The one-tissue model showed a lack of fit in low-binding regions, and the two-tissue model failed to estimate parameters reliably. Regional time–activity curves were well described by MA1. The rank order of [^{11}C]AFM binding potential (BP_{ND}) matched well with the known regional SERT densities. For routine use of [^{11}C]AFM, several noninvasive methods for quantification of regional binding were evaluated, including simplified reference tissue models (SRTM and SRTM2), and multilinear reference tissue models (MRTM and MRTM2). The best methods for region of interest (ROI) analysis were MA1, MRTM2, and SRTM2, with fixed population kinetic values (k'_2 or b') for the reference methods. The MA1 and MRTM2 methods were best for parametric imaging. These results showed that [^{11}C]AFM is a suitable PET radioligand to image and quantify SERT in humans.

Journal of Cerebral Blood Flow & Metabolism (2013) **33**, 1886–1896; doi:10.1038/jcbfm.2013.134; published online 7 August 2013

Keywords: brain imaging; dopamine; 5-HT; kinetic modeling; positron emission tomography; receptor imaging

INTRODUCTION

The serotonin transporter (SERT) is located on the presynaptic terminals of neurons, and is responsible for the reuptake of serotonin, a neurotransmitter involved in the regulation of brain functions such as mood, appetite, and sleep.¹ Serotonin transporter is a primary target of action for selective serotonin reuptake inhibitors, which are effective therapeutic agents for the treatment of major depressive disorder, obsessive-compulsive disorder, posttraumatic stress disorder, and other mood and anxiety disorders. Because the serotonin system has such an important role in the pathophysiology of these diseases, there has been considerable interest in developing *in vivo* positron emission tomography (PET) radioligands for imaging SERT distribution. In the human brain, highest concentrations of SERT are found in the raphe nucleus and midbrain, followed by thalamus, striatum, and amygdala. Intermediate levels are in the limbic system (hippocampus and cingulate cortex), and lower levels in the neocortex regions, with cerebellum displaying lowest to negligible SERT density.^{2–5}

Over the years, a number of high-affinity ligands have been developed for SERT imaging with PET. [^{11}C]McN5652 [^{11}C]McN5652 (trans-1,2,3,5,6,10 β -hexahydro-6-[4- ^{11}C](methylthio)phenyl]-pyrrolo-[2,1-a]-isoquinoline)⁶ was the first successful and widely used tracer. However, [^{11}C]McN5652 has many limitations, which include high nonspecific binding, nonmeasurable free

fraction in the plasma (<1%), and long scanning time (120 minutes). Because of high-nonspecific binding, this tracer does not provide reliable quantification in brain regions with moderate and low SERT densities. Given these limitations and the need for SERT tracers with improved imaging properties, a number of ligands derived from diphenyl sulfides were developed [^{11}C]DASB ([^{11}C]N,N-dimethyl-2-(2-amino-4-cyanophenylthio)benzylamine),⁷ [^{11}C]AFM ([^{11}C]2-[2-(dimethylaminomethyl)phenylthio]-5-fluoromethylphenylamine),⁸ [^{11}C]ADAM ([^{11}C]2-((dimethylamino)methyl)phenylthio)-5-iodophenylamine),⁹ [^{11}C]DAPA ([^{11}C]5-bromo-2-[2-(dimethylaminomethylphenylsulfanyl)]phenylamine)¹⁰. In a comparative evaluation of these tracers and [^{11}C]McN5652, both [^{11}C]DASB and [^{11}C]AFM were shown to be superior radioligands to image SERT in baboons, with [^{11}C]DASB displaying fastest brain kinetics that enabled the measurement of SERT availability in a shorter scanning time, and [^{11}C]AFM having the highest specific-to-nonspecific binding ratios (BP_{ND}).¹¹ The plasma free fraction for [^{11}C]DASB and [^{11}C]AFM was high enough to be reliably measured. Since then, [^{11}C]DASB has become the most widely used 'standard' tracer. Subsequently, [^{11}C]MADAM ([^{11}C]N,N-dimethyl-2-(2'-amino-4'-methylphenylthio)benzylamine)¹² and [^{11}C]HOMADAM ([^{11}C]N,N-dimethyl-2-(2'-amino-4'-hydroxymethylphenylthio)benzylamine)¹³ were also developed and evaluated in humans.^{14,15} Like [^{11}C]AFM in baboons, [^{11}C]MADAM and [^{11}C]HOMADAM appeared to have

¹Diagnostic Radiology, PET Center, Yale University School of Medicine, New Haven, Connecticut, USA and ²Department of Psychiatry and Radiology, New York University School of Medicine, New York, NY, USA. Correspondence: Dr M Naganawa, Diagnostic Radiology, PET Center, Yale University School of Medicine, PO Box 208048, New Haven, CT 06520-8048, USA.

E-mail: mika.naganawa@yale.edu

This work was supported by NIMH (MH066624) and Grant-in-Aid for Young Scientists (B) (21791232). This publication was also made possible by CTSA Grant Number UL1 RR024139 from the National Center for Research Resources (NCRR), a component of the National Institutes of Health (NIH), and NIH roadmap for Medical Research. Its contents are solely the responsibility of the authors and do not necessarily represent the official view of NCRR or NIH.

Received 9 February 2013; revised 11 July 2013; accepted 12 July 2013; published online 7 August 2013

higher BP_{ND} than [¹¹C]DASB in humans, even though these comparisons were not made within subjects. High BP_{ND} might allow more reliable measurement of SERT availability in brain regions, especially cortical regions, where SERT concentrations are low, but SERT abnormalities have been observed in several postmortem studies of patients with psychiatric disorders.¹⁶ Thus, to investigate SERT in cortical regions, tracers with better imaging characteristics than [¹¹C]DASB are needed.

[¹¹C]AFM is a potential PET radioligand that could measure the SERT in both high- and low-density regions. Here we report the first human PET study with [¹¹C]AFM to evaluate its pharmacokinetics and brain distribution and to develop appropriate kinetic modeling techniques for the quantitative analysis of its binding parameters.

MATERIALS AND METHODS

Human Subjects

Positron emission tomography scans were performed in 10 healthy volunteers whose age ranged from 20 to 45 years (6 men, 4 women). This study was performed under a protocol approved by the Human Investigation Committee, Yale University School of Medicine, and the Yale-Haven Hospital Radiation Safety. Written informed consent was obtained from all subjects. This study was performed according to the Ethical Principles and Guidelines for the Protection of Human Subjects of Research (Belmont Report).

As part of the subject evaluation, magnetic resonance (MR) images were acquired on all subjects to eliminate those with structural brain abnormalities and for image registration. Magnetic resonance imaging was performed on a 3T whole-body scanner (Trio; Siemens Medical Systems, Erlangen, Germany) with a circularly polarized head coil. The dimension and pixel size of MR images were $256 \times 256 \times 176$ and $0.98 \times 0.98 \times 1.0$ mm³, respectively.

Radiochemistry

[¹¹C]AFM was prepared using the TRACERLab™ FXC automated synthesizer (GE Healthcare, Chalfont St Giles, UK) by *N*-methylation of the desmethyl precursor with [¹¹C]methyl triflate instead of [¹¹C]methyl iodide as previously reported using a manual method.⁸ Briefly, [¹¹C]methyl triflate was trapped at 0°C in a solution of 0.5 to 1 mg precursor in 400 μL of anhydrous methyl ethyl ketone. The mixture was then heated for 1 minute at 60°C, and then purified by reverse-phase semipreparative high-performance liquid chromatography (HPLC). The HPLC fraction containing the product was further purified by solid-phase extraction and formulated in ethanol and saline into a sterile solution ready for administration. Radiochemical purity of the final product was $93.0 \pm 1.5\%$. (see Supplementary Data and Supplementary Figure S1 for further details).

Positron Emission Tomography Scanning Procedure

Positron emission tomography scans were performed on the high-resolution research tomography (HRRT) (Siemens Medical Solutions, Knoxville, TN, USA), which acquires 207 slices (1.2-mm slice separation) with a reconstructed image resolution of ~3 mm. Before tracer administration, a 6-minute transmission scan was conducted for attenuation correction. [¹¹C]AFM (dose: 712 ± 47 MBq; specific activity at the time of injection: 193 ± 127 GBq/μmol) was administered intravenously over 1 minute by an automatic pump (Harvard PHD 22/2000; Harvard Apparatus, Holliston, MA, USA), and a 120-minute PET scan was acquired in list mode. Dynamic scan data were reconstructed in 33 frames (6×0.5 minutes, 3×1 minutes, 2×2 minutes, and 22×5 minutes) with all corrections (attenuation, normalization, scatter, randoms, and deadtime) using the MOLAR algorithm.¹⁷ Motion correction was included in the reconstruction based on measurements with the Polaris Vicra sensor (NDI Systems, Waterloo, ON, Canada) with reflectors mounted on a swim cap worn by the subject.

Input Function Measurement

For each study, a catheter was inserted into the subject's radial artery for blood sampling. An automated blood counting system (PBS-101; Veenstra Instruments, Joure, The Netherlands) was used to measure the radioactivity in whole blood during the first 7 minutes, with blood withdrawn continuously at 4 mL/min. Thereafter, 15 samples (1 to 6 mL) were

collected manually at 3, 5, 7, 10, 15, 20, 25, 30, 40, 50, 60, 75, 90, 105, and 120 minutes after tracer administration. For each sample, plasma was obtained by refrigerated centrifugation (2930 *g* at 4°C for 5 minutes). Whole blood and plasma were counted in cross-calibrated gamma counters (1480 WIZARD; Perkin-Elmer, Waltham, MA, USA).

To determine radioactivity in the plasma for the first 7 minutes, the whole blood-to-plasma ratios ($r(t)$) were calculated from the hand-drawn samples. The ratios between 3 and 120 minutes were fitted to the following equation: $r(t) = a \exp(bt) + c$, and the plasma time-activity curve (TAC) in the first 7 minutes was calculated from the measured whole blood TAC and the extrapolated ratio. These data were combined with the plasma samples to produce the final curve of total radioactivity in the plasma. To reduce noise in these data, the total plasma curve from ~6 minutes onward was fitted to a sum of exponentials.

Plasma Metabolite and Protein-Binding Analysis

Metabolism of the radiotracer was analyzed with arterial blood samples collected at 3, 7, 15, 30, 60, and 90 minutes after tracer injection, using the column-switching HPLC method.¹⁸ Plasma samples were first treated with urea (8 mol/L) and citric acid (50 mmol/L), and then loaded onto a capture column (19×4.6 mm²) packed with Phenomenex SPE C18 Strata-X sorbent and eluting with 1% acetonitrile in water at a flow rate of 2 mL/min. At 4 minutes after sample injection, the activity on the capture column was back flushed onto an analytical column (Phenomenex Luna Phenyl hexyl, Torrance, CA, USA; 5 μm, 250×4.6 mm²) eluting with 30% acetonitrile in 0.1 mol/L ammonium formate at a flow rate of 1.50 mL/min. The HPLC eluent was collected with an automated fraction collector and the fractions were counted with an automatic gamma well counter (Wizard 1480; Perkin-Elmer). The unmetabolized parent fraction was determined as the ratio of the sum of radioactivity in fractions containing the parent tracer to the total amount of radioactivity collected, and fitted with bounded sum of exponentials. The final plasma input function was calculated as the product of the total plasma curve and the parent fraction curve.

Ultrafiltration-based method was used for measuring the unbound portion (free fraction, f_p) of [¹¹C]AFM in the plasma. [¹¹C]AFM (~6 MBq) was mixed with arterial blood (6 mL) taken immediately before tracer injection. After standing for 10 minutes at room temperature, the spiked blood sample was centrifuged at 2930 *g* for 5 minutes to separate the plasma. Plasma aliquots (0.3 mL) were then taken and loaded onto the reservoir of the Millipore Centrifree micropartition device in triplicate and centrifuged at 1228 *g* for 20 minutes. The free fraction f_p was determined from the activity ratio of ultrafiltrate to plasma. Similarly, the amount of nonspecific binding of [¹¹C]AFM to the filter was also determined as described above by spiking a sample of saline with [¹¹C]AFM. The ultrafiltrate to spiked saline ratio was 0.96 ± 0.03 ($n = 10$), indicating negligible tracer retention on the filter.

Image Registration and Regions of Interest

Regions of interest (ROI) were taken from the automated anatomic labeling (AAL) for SPM2¹⁹ in Montreal Neurological Institute (MNI) space.²⁰ For each subject, the dynamic PET images after hardware motion correction were coregistered to the early summed PET images (0 to 10 minutes after injection) using a six-parameter mutual information algorithm²¹ (FMRIB's Linear Image Registration Tool, FMRIB Software Library) to eliminate any residual uncorrected motion. The summed PET images were then coregistered to the subject's T1-weighted 3T MR images (six-parameter affine registration), which were subsequently coregistered to the AAL template in MNI space using a 12-parameter affine transformation. Using the combined transformation from template to PET space, TACs were generated for 13 ROIs: amygdala, caudate, cerebellum, anterior cingulate, posterior cingulate, frontal lobe, hippocampus, occipital lobe, putamen, midbrain raphe, pontine raphe, temporal lobe, and thalamus. The raphe regions (0.64 mL for midbrain raphe, and 0.21 mL for pontine raphe) were added to the standard AAL template as described previously.²² In this study, we used a portion of the cerebellum region located at the inferior end, based on a blocking study with citalopram, which showed minimal blockade (<15%).²³ The ROIs were *a priori* divided into four categories: regions with very high SERT density (raphe regions), regions of high density (thalamus, putamen, caudate, amygdala), regions of intermediate density (hippocampus, cingulate cortex), and regions of low density (neocortices).

Kinetic Modeling

Compartment models with the arterial input function. Kinetic analysis of tissue data was performed with the one-tissue (1T) and two-tissue (2T) compartment models.²⁴ The rate constants, K_1 and k_2 for the 1T model and K_1 , k_2 , k_3 , and k_4 for the 2T model, were estimated by weighted nonlinear least squares (see below). The primary outcome measure was the total volume of distribution, V_T .²⁵ Three versions of the binding potential were then computed from the V_T values: $BP_{ND} = V_T/V_{ND} - 1$, $BP_P = V_T - V_{ND}$, and $BP_F = (V_T - V_{ND})/f_p$.²⁵ Here the cerebellum gray matter was used as the reference region. Previous studies reported extremely low^{2,3} or low^{4,5,26} SERT density in the cerebellum.

Graphical analysis with the arterial input function. The multilinear analysis-1 (MA1) method²⁷ was applied for [¹¹C]AFM quantification using the measured input function. The MA1 method is intermediate between 1T and 2T models. When the TAC is described well by the 1T model, early t^* setting for MA1 provides small bias in the estimate. Conversely, when the TAC is described well by the 2T model, late t^* setting will help minimize bias, although stability of parameter estimates must also be considered. The equation for MA1 is:

$$C_T(T) = -\frac{V_T}{b} \int_0^T C_P(t) dt + \frac{1}{b} \int_0^T C_T(t) dt \quad (T > t^*) \quad (1)$$

where C_T is the tissue curve and C_P is the metabolite-corrected input function.

Effect of scan duration on V_T estimates. The effect of scan duration on parameter stability was calculated by shortening the fitting interval. Scan durations ranging from 70 to 120 minutes were evaluated. For each region and duration, the ratio of the estimated V_T values to the 120-minute values was calculated. The following two criteria were used to select optimal scan duration²⁸: (a) the average of this ratio was between 0.95 and 1.05; and (b) the intersubject s.d. of this ratio was <0.1 .

Reference tissue compartment models. Reference tissue models use a TAC from the reference region, $C_{REF}(t)$, instead of the input function. The simplified reference tissue model (SRTM)²⁹ is described with the equation:

$$C_T(t) = R_1 C_{REF}(t) + R_1 (k_2' - k_2) C_{REF}(t) \otimes \exp(-k_2 t) \quad (2)$$

where k_2 and k_2' are the efflux rate constants from the target and the reference regions, respectively, and R_1 is the ratio of influx constants K_1 between target and reference regions. The SRTM method assumes that all regions can be described by a 1T model and has three parameters to estimate. The parameter k_2' should be common among all regions or voxels. However, a different value of k_2' is estimated by equation (2) for each voxel. The two-parameter version of SRTM³⁰ (SRTM2) was also applied. The two-parameter method has been shown to be effective in reducing noise from the original three-parameter models. The use of SRTM2 requires fixing k_2' with a preliminary analysis. Approaches to fix this parameter for [¹¹C]AFM are described below.

Graphical analyses with reference region. The multilinear reference tissue model (MRTM),³¹ which is based on graphical analysis, was evaluated. The equation for MRTM is described as:

$$C_T(T) = -\frac{1}{b} \frac{V_T}{V_T'} \int_0^T C_{REF}(t) dt + \frac{1}{b} \int_0^T C(t) dt + \frac{b' V_T}{b V_T'} C_{REF}(T) \quad (T > t^*) \quad (3)$$

The MRTM method has three parameters to estimate. Like SRTM, MRTM has a two-parameter version: MRTM2.³¹ The use of MRTM2 requires fixing b' ($= -1/k_2'$ for 1T model) from a preliminary analysis. Approaches to determine the value of b' are described below.

Determination of reference region parameters for simplified reference tissue model 2 and multilinear reference tissue model 2. In the reference tissue models that fix one parameter, two approaches were evaluated:

Coupled fit: All TACs were fitted simultaneously under the constraint of finding a common parameter (k_2' or b') to all regions in SRTM2 and MRTM2, i.e., parameter coupling.³²

Population value: The value of k_2' or b' was fixed to the population average values estimated from the 1T model (SRTM2) or MA1 models

(MRTM2). To differentiate from the coupled fit, a model with population value is denoted with the suffix 'pop' (e.g., SRTM2pop).

For all reference region fits, to reduce estimation error, the reference region TAC was fitted by a sum of exponentials (1 to 3 exponentials; the number of exponentials was selected by minimizing χ^2) starting from ~ 25 minutes after injection.

Selection of start of fitting period (t^*) for graphical analyses. The effect of the choice of starting time (t^*) for graphical analyses was evaluated by varying t^* from 10 to 60 minutes after injection in 10-minute increments. The determination of t^* for MA1 was conducted by visual inspection of fit quality. After selecting the best t^* for MA1 (40 minutes, see Results), the optimal t^* for MRTM and MRTM2 were selected by comparing the values of MRTM and MRTM2 BP_{ND} with the MA1 BP_{ND} estimates.

Parametric Imaging

Parametric imaging was performed using 1T, MA1, SRTM, SRTM2, MRTM, and MRTM2. A basis function method was used for parametric imaging for the compartmental methods where the range of k_2 for the basis functions was $0.005 \leq k_2 \leq 1/\text{min}$. Region of interests were applied to the parametric images and these values were compared between methods and with the values obtained by MA1 fits ($t^* = 40$ minutes) of the ROI TACs. For the SRTM2 or MRTM2 calculation, the value k_2' or b' was fixed to a global value among all voxels. The SRTM (or MRTM) method was applied to estimate k_2' (or b') from all brain voxels. Then, the global value was computed as the median of k_2' or b' estimates from selected brain voxels ($BP_{ND} > 0.5$). The effect of smoothing to reduce noise before estimation was investigated by applying a three-dimensional Gaussian filter with full-width at half-maximum (FWHM) of 3.6 and 6.0 mm (3 and 5 voxels) to the original image data.

Implementation

For all approaches, kinetic parameters were estimated using weighted least squares, with the weights determined based on noise equivalent counts in each frame. A Marquardt-Levenberg algorithm was used for nonlinear least-squares estimation applied to ROI TACs. Estimates of relative standard error (rSE) of the parameters were derived from the covariance matrix. Time shifts between blood and brain were estimated by applying the 1T model to the whole brain TAC and these values were then used as a global correction for all analyses. All methods were implemented with IDL 8.0 (ITT Visual Information Solutions, Boulder, CO, USA).

Statistics

Goodness of fit was evaluated by visual inspection, and by calculating χ^2 statistics, the Akaike information criterion,³³ the Schwartz criterion,³⁴ and the F test using the weighted residual sum of squares. Statistical significance using the F test was assessed with $P < 0.05$.

RESULTS

Arterial Input Function

Figure 1A shows a typical example of the radioactivity concentration in the plasma over time. In most cases, the whole blood to plasma ratio was >1 for the first 20 minutes (1.22 ± 0.14 at 5 minutes, $n = 10$), and subsequently decreased (0.82 ± 0.03 at 90 minutes, $n = 10$). This pattern was similar to that of [¹¹C]DASB.³⁵ The plasma free fraction (f_p) of [¹¹C]AFM was $8.6 \pm 1.8\%$ ($n = 10$), which was similar to that in baboons ($9.6 \pm 0.5\%$, $n = 4$).¹¹ [¹¹C]AFM was rapidly metabolized, and the parent fraction was $47 \pm 5\%$, $37 \pm 4\%$, $24 \pm 4\%$, $8 \pm 2\%$, and $3.8 \pm 1.4\%$ at 7, 15, 30, 60, 90 minutes after injection, respectively. Figure 1B shows the average parent fraction over time and the fitted curve averaged over all subjects. The rapid clearance and metabolism of [¹¹C]AFM required careful handling to avoid low statistical quality of the metabolite data at later sampling times. AFM metabolites in arterial plasma were polar in comparison with the parent. Examples of the HPLC results are shown in the Supplementary Data (Supplementary Figure S2).

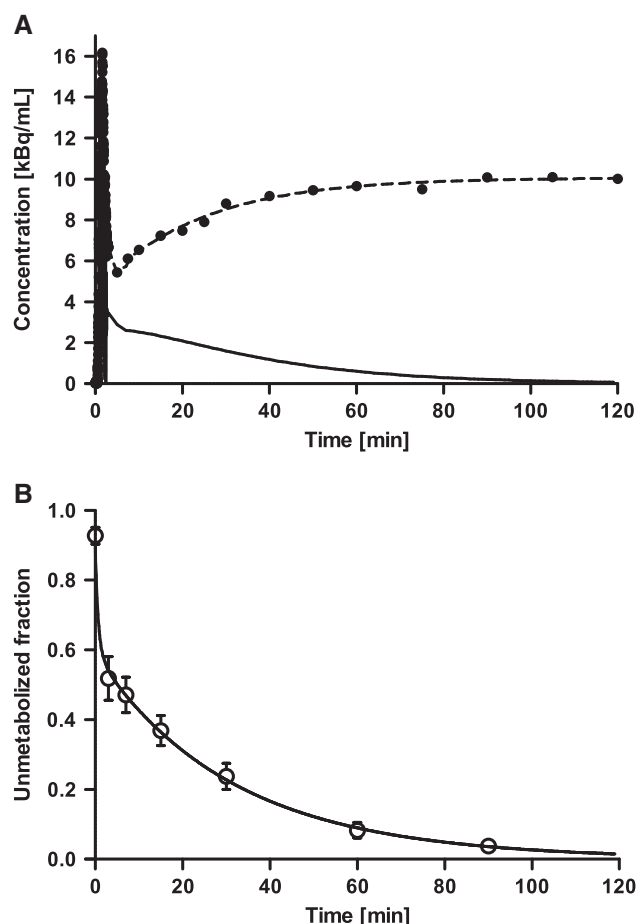


Figure 1. (A) Typical example of time-activity curves of total radioactivity in the plasma (dots) and its fit (dashed line), and the corresponding metabolite-corrected input curve (solid line). (B) Mean \pm s.d. of unmetabolized [¹¹C]AFM ([¹¹C]2-[2-(dimethylaminoethyl)phenylthio]-5-fluoromethylphenylamine) fraction over time in 10 healthy human subjects and mean of fitted curve (solid line). The parent fraction was fitted using a sum of exponentials.

Region of Interest Data Analysis

Regional TACs. Figures 2A and 2B shows typical TACs from the 13 ROIs. Radioactivity concentrations were highest in the raphe regions and high levels were seen in the putamen, thalamus, caudate, and amygdala. Intermediate levels of activity were observed in the hippocampus and anterior cingulate cortex, with lower levels in the posterior cingulate and other cortical regions, as well as the cerebellum. In the cerebellum region, the concentration peaked at \sim 30 minutes after injection. The peak times were similar in regions with low SERT densities. Regions with higher densities peaked at later times (50 to 70 minutes). The data from raphe, a high-density, small region, were too noisy to obtain stable parameter estimates. On average, pontine raphe and midbrain raphe peaked at around 80 minutes, and then slightly decreased.

Compartmental modeling with the input function. In most cases, the 2T model converged and fitted the data well; however, the parameter values were often implausible (e.g., $k_3 < 10^{-3}$ /min, $V_T > 500$ mL/cm³). Such implausible parameters were seen mainly in neocortical regions across most subjects. In addition, for two subjects, questionable parameters were seen in most regions.

Results obtained from the 1T model are presented in Table 1. Figures 2A and 2B show representative fits to the 1T model in one

subject, chosen as the subject with best correlation of individual V_T values to the population average values (Table 1). Convergence was achieved for all regions using the 1T model. Visual inspection of 1T fitting showed some lack of fit in regions with intermediate to low binding, with nonrandom distribution of the residuals. In those cases, the fitted curve tended to overestimate the data at intermediate time points (\sim 30 minutes), and underestimate it at late time points (\sim 90 minutes). In high-binding regions, 1T fitting was good.

The uptake rate constant K_1 ranged from 0.42 to 0.68 mL/min per cm³ reflecting moderate to high extraction of [¹¹C]AFM. The K_1 value had an rSE of $<6\%$ (mean 2%) in all regions except for the raphe. The rate constant k_2 had an rSE of $<8\%$ (mean 3%), excluding the raphe. V_T and BP_{ND} values were estimated with rSE of $<7\%$ (mean 2%) and $<10\%$ (mean 4%) (except for raphe regions), respectively. Excluding the raphe, the order of V_T values from the 1T model was: amygdala $>$ putamen $>$ thalamus $>$ caudate $>$ hippocampus \approx anterior cingulate cortex $>$ posterior cingulate cortex \approx occipital lobe $>$ temporal lobe $>$ frontal lobe $>$ cerebellum. Estimates of V_T and BP_{ND} are presented in Tables 1 and 2.

The parameters in the raphe regions showed large intersubject variability, and rSE for V_T and BP_{ND} were $>20\%$. The combination of small size and slow kinetics in the raphe leads to a noisy TAC and unstable estimation. Therefore, the raphe regions were excluded from further analysis.

Graphical analyses with the input function. Representative fitting plots using MA1 with starting times for fitting t^* set to 10 and 40 minutes are displayed in Figures 2C and 2D, respectively. Visual inspection of the MA1 fitting with early t^* (10 to 30 minutes) showed a similar pattern of lack of fit to the 1T model. MA1 fitting was improved by increasing t^* to 40 minutes, as shown in Figure 2D.

Supplementary Figure S3 shows the V_T values from MA1 with different t^* . When t^* was increased, V_T estimates increased in the cerebellum and other regions with low SERT densities. However, in regions with high densities, the estimates slightly decreased with larger t^* . For example, with $t^* = 40$ minutes, V_T values increased by 6% in the cerebellum and decreased by 3% in the amygdala when compared with $t^* = 10$ minutes. The values of BP_{ND} were therefore decreased with increasing t^* in all regions. Based on visual inspection, $t^* = 40$ minutes was selected for use in further analysis.

The MA1 estimates of V_T and BP_{ND} are presented in Tables 1 and 2. The MA1 method provided values of V_T similar to those derived from 1T model in high-binding regions, whereas in intermediate and low-binding regions, MA1 provided higher values of V_T . V_T estimates using MA1 matched well with V_T estimates using the 2T model ($V_T(\text{MA1}, t^* = 40 \text{ minutes}) = 0.97 V_T(2T) - 0.87$, $r^2 = 0.98$). Note that estimates with 2T %SE > 10 (54 out of 110 fits) were excluded from this comparison. Because of this stronger bias observed with 1T in the cerebellum and low-binding regions, BP_{ND} estimates from the MA1 method were smaller than those from 1T. For MA1, estimates of the intercept b ranged from -103 ± 27 minutes in the amygdala to -28 ± 4 minutes in the cerebellum. BP_{ND} values ranged from 0.57 ± 0.06 in the frontal lobe to 3.1 ± 0.7 in the amygdala. The correlation scatter plot and regression line between BP_{ND} estimates from 1T and MA1 are shown in Figure 3A.

The three binding potentials, BP_{ND} , BP_p , and BP_f using MA1, are presented in Table 2. These three outcome measures were well correlated with one another. Regional BP_p and BP_f values in general displayed larger intersubject variability than BP_{ND} . Average values for each variability were 14%, 20%, and 24% for BP_{ND} , BP_p , and BP_f , respectively. For MA1 with $t^* = 40$ minutes, the tissue free fraction (f_{ND}) calculated from the cerebellum V_T and f_p was 0.008 ± 0.002 . No significant correlation was found between the

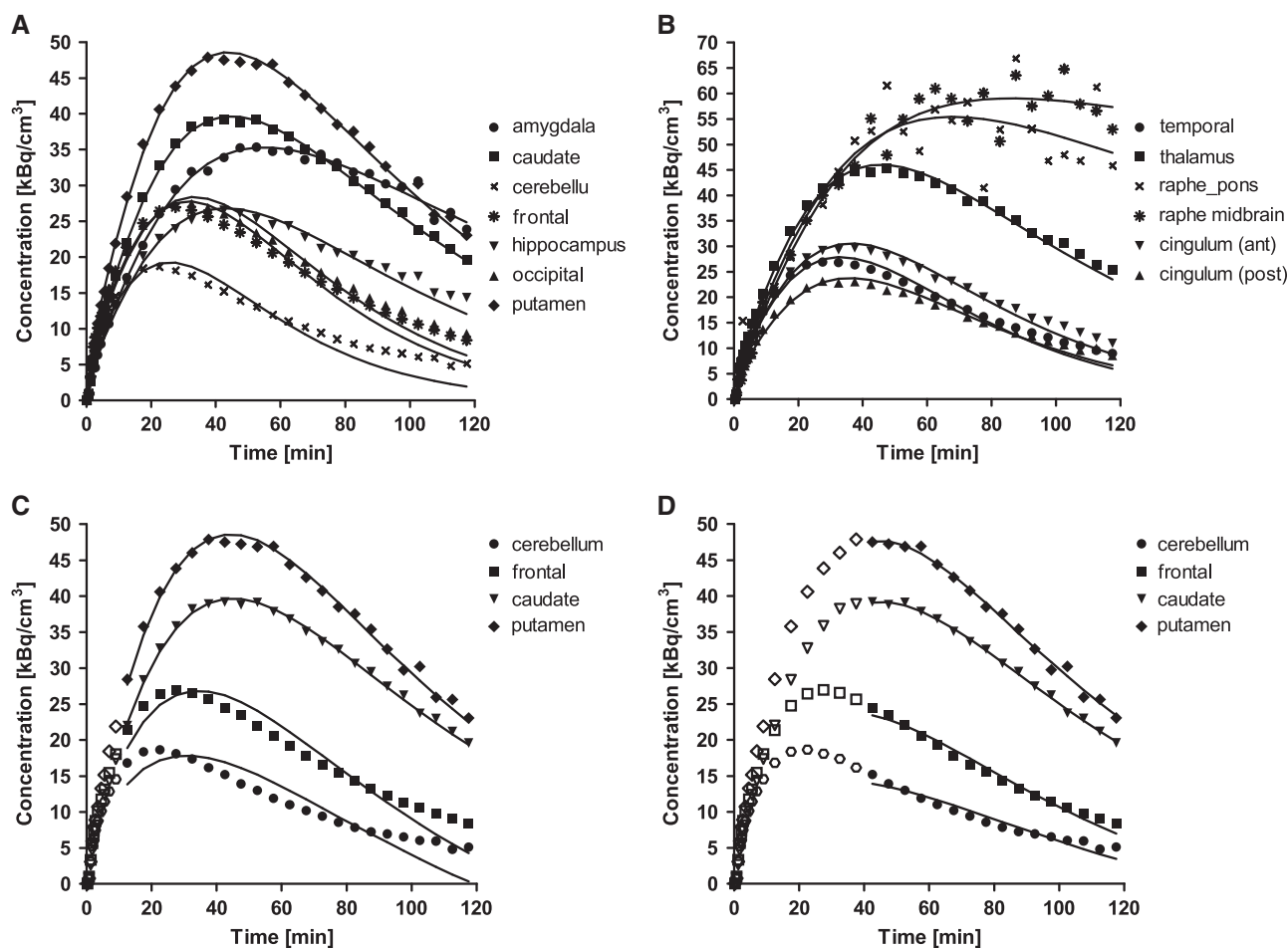


Figure 2. Typical time activity curves in 13 region of interest (ROIs) measured after injection of 700 MBq of [¹¹C]AFM ([¹¹C]-2-(dimethylaminomethyl)phenylthio]-5-fluoromethylphenylamine). For each region, the symbols correspond to the measured activities and the lines are values fitted to one-tissue compartment model. Curves are shown in two graphs (A and B) for clarity, using different scales. Typical examples of fitting are shown for multilinear analysis with (C) $t^* = 10$ minutes and (D) $t^* = 40$ minutes. ROIs are cerebellum (circles, ●), frontal lobe (triangles, ▲), caudate (downward-pointing triangles, ▼), and putamen (diamonds, ◆). Points used for the estimation are shown in closed symbols.

measured free fraction f_p and V_{ND} ($r^2 = 0.26$, $n = 10$, Student's t -test, $P = 0.13$), suggesting why correction for f_p does not reduce intersubject variability.

Effect of scan duration on parameter estimates. Time-activity curves were fitted for different scan durations, to define the minimum scan time required for reliable estimates of binding parameters. Using comparatively strict criteria, minimal scanning time ranged between 70 to 90 minutes (Table 1). The mean V_T values in high-binding regions did not change with decreasing scan duration (see Supplementary Figure S4).

Compartmental modeling without input function. Typical fits using SRTM and SRTM2pop are presented in Figures 4A and 4B. The values of k_2 in SRTM ($0.095 \pm 0.020/\text{min}$) and SRTM2 ($0.096 \pm 0.017/\text{min}$) were larger than the population value of k_2 from 1T in the cerebellum ($0.053/\text{min}$). Visual inspection indicates that SRTM and SRTM2 provide better quality of fit than SRTM2pop. The SRTM method was compared with SRTM2pop using the F test, which showed that weighted residual sum of squares of SRTM was significantly smaller than that of SRTM2pop in almost all fits (98 out of 100 fits). The correlation scatter plot and regression line between BP_{ND} estimates from SRTM2, and SRTM2pop and MA1 with $t^* = 40$ minutes are shown in

Supplementary Figures S5B and S5C, respectively. Simplified reference tissue model BP_{ND} showed a very similar regression line to SRTM2 BP_{ND} (Supplementary Figure S5). The SRTM and SRTM2 BP_{ND} estimates were smaller than MA1 estimates. In spite of the lack of fits, BP_{ND} estimates from SRTM2pop were similar to MA1 estimates. Presumably, the lack of fit with SRTM2pop is because of the inadequacy of 1T fitting in low-binding regions (Figure 2A). Intersubject variability of BP_{ND} was similar among SRTM, SRTM2, and SRTM2pop.

Graphical analyses without input function. Typical fits using MRTM and MRTM2pop are presented in Figures 4C and 4D, respectively. The value of t^* was set to 40 minutes after injection. The comparison between BP_{ND} values obtained from MRTM2, and MRTM2pop, and MA1 is presented in Supplementary Figure S5I and Figure 3B, respectively. Multilinear reference tissue model BP_{ND} showed a very similar regression line to SRTM BP_{ND} (Supplementary Figure S5). The value of b' was not constant among regions in MRTM, but the interregion average (-26 ± 13 minutes) was similar to the population value of b from MA1 model in the cerebellum (-28 minutes). As seen with SRTM and SRTM2, the MRTM and MRTM2 BP_{ND} estimates were smaller than MA1 estimates (Supplementary Figure S5). The MRTM2pop method provided BP_{ND} estimates similar to those from MA1, as

Table 1. Kinetic parameters estimated from 1T compartment model and MA1

Regions	V_T (mL/cm ³) ^a		K_1 (mL/min per cm ³) ^a	k_2 (1/min) ^a	Minimal scan duration (min)
	1T	MA1 ^b			
Cerebellum	9.7 (20%)	10.6 (19%)	0.52 (24%)	0.053 (10%)	90
Amygdala	44.2 (29%)	42.9 (23%)	0.42 (20%)	0.010 (22%)	80
Putamen	40.8 (17%)	41.0 (17%)	0.68 (23%)	0.017 (13%)	70
Thalamus	39.4 (21%)	40.3 (21%)	0.66 (20%)	0.017 (11%)	70
Caudate	33.2 (13%)	32.9 (12%)	0.56 (21%)	0.017 (15%)	70
Hippocampus	21.2 (24%)	22.3 (24%)	0.42 (18%)	0.020 (13%)	80
Ant. cingulate cortex	21.5 (18%)	22.3 (17%)	0.56 (26%)	0.026 (17%)	70
Post. cingulate cortex	17.1 (19%)	17.8 (18%)	0.53 (24%)	0.031 (12%)	80
Occipital lobe	16.9 (21%)	17.7 (20%)	0.58 (22%)	0.034 (12%)	80
Temporal lobe	16.2 (16%)	17.0 (15%)	0.55 (20%)	0.034 (11%)	80
Frontal lobe	15.7 (18%)	16.6 (18%)	0.58 (23%)	0.037 (11%)	80
Raphe midbrain	231.8 (127%)	151.1 (47%)	0.48 (17%)	0.004 (46%)	
Raphe pons	124.8 (91%)	100.1 (52%)	0.57 (21%)	0.007 (48%)	

COV, coefficients of variation; 1T, one-tissue; MA1, multilinear analysis-1.

^aValues are means (%COV, intersubject variability) in 10 subjects. ^b t^* was set to 40 minutes after injection.

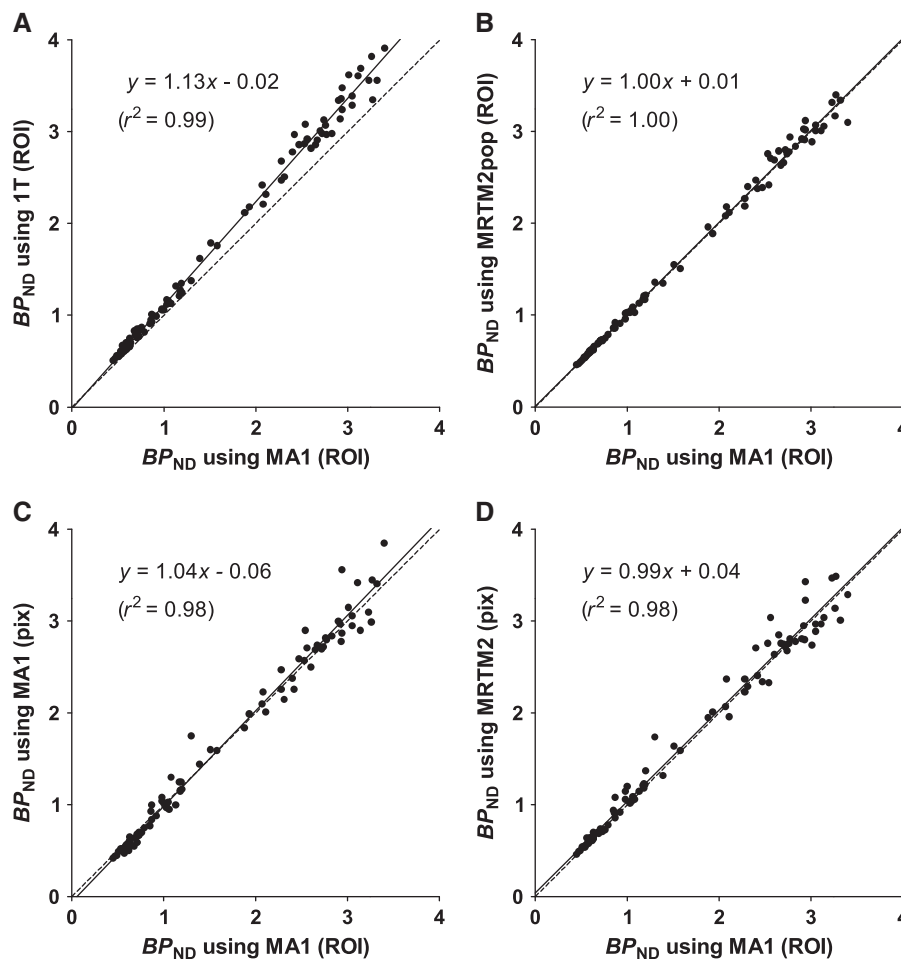


Figure 3. Comparison of binding potential (BP_{ND}) values between region of interest (ROI) analysis with multilinear analysis-1 (MA1) ($t^* = 40$ minutes) and other ROI analyses and parametric image methods. For parametric imaging, a three-dimensional Gaussian filter with full-width at half-maximum = 3.6 mm was applied to the dynamic image data. The reference region was the cerebellum. Raphe regions were excluded from this analysis. The line of identity (dotted line) is added to each panel for reference. Region of interest analyses using (A) one-tissue (1T) compartment model and (B) two-parameter multilinear reference tissue model (MRTM2) with a population value of b' , and parametric images using (C) MA1 and MRTM2. The value of t^* was set to 40 minutes after injection in panels B, C, and D.

Table 2. Comparison of binding potential values between the 1T compartment model and MA1

Regions	BP_{ND}^a		$BP_F(mL/cm^3)^a$	
	1T	MA1 ^b	MA1 ^b	MA1 ^b
Amygdala	3.60 (34%)	3.07 (24%)	32.29 (26%)	393 (35%)
Putamen	3.25 (11%)	2.89 (8%)	30.43 (17%)	365 (19%)
Thalamus	3.08 (13%)	2.81 (12%)	29.76 (23%)	352 (18%)
Caudate	2.49 (16%)	2.14 (14%)	22.31 (13%)	270 (23%)
Hippocampus	1.19 (21%)	1.10 (20%)	11.71 (31%)	140 (30%)
Ant. cingulate cortex	1.23 (14%)	1.12 (12%)	11.72 (17%)	141 (22%)
Post. cingulate cortex	0.77 (16%)	0.69 (17%)	7.21 (21%)	86 (21%)
Occipital lobe	0.74 (10%)	0.67 (10%)	7.09 (23%)	84 (21%)
Temporal lobe	0.69 (17%)	0.62 (16%)	6.41 (15%)	78 (27%)
Frontal lobe	0.63 (10%)	0.57 (10%)	6.02 (18%)	72 (22%)
Raphe midbrain	24.0 (141%)	13.62 (55%)	140.49 (50%)	1769 (61%)
Raphe pons	12.5 (107%)	8.84 (67%)	89.47 (58%)	1143 (72%)

COV, coefficients of variation; 1T, one tissue; MA1, multilinear analysis-1.

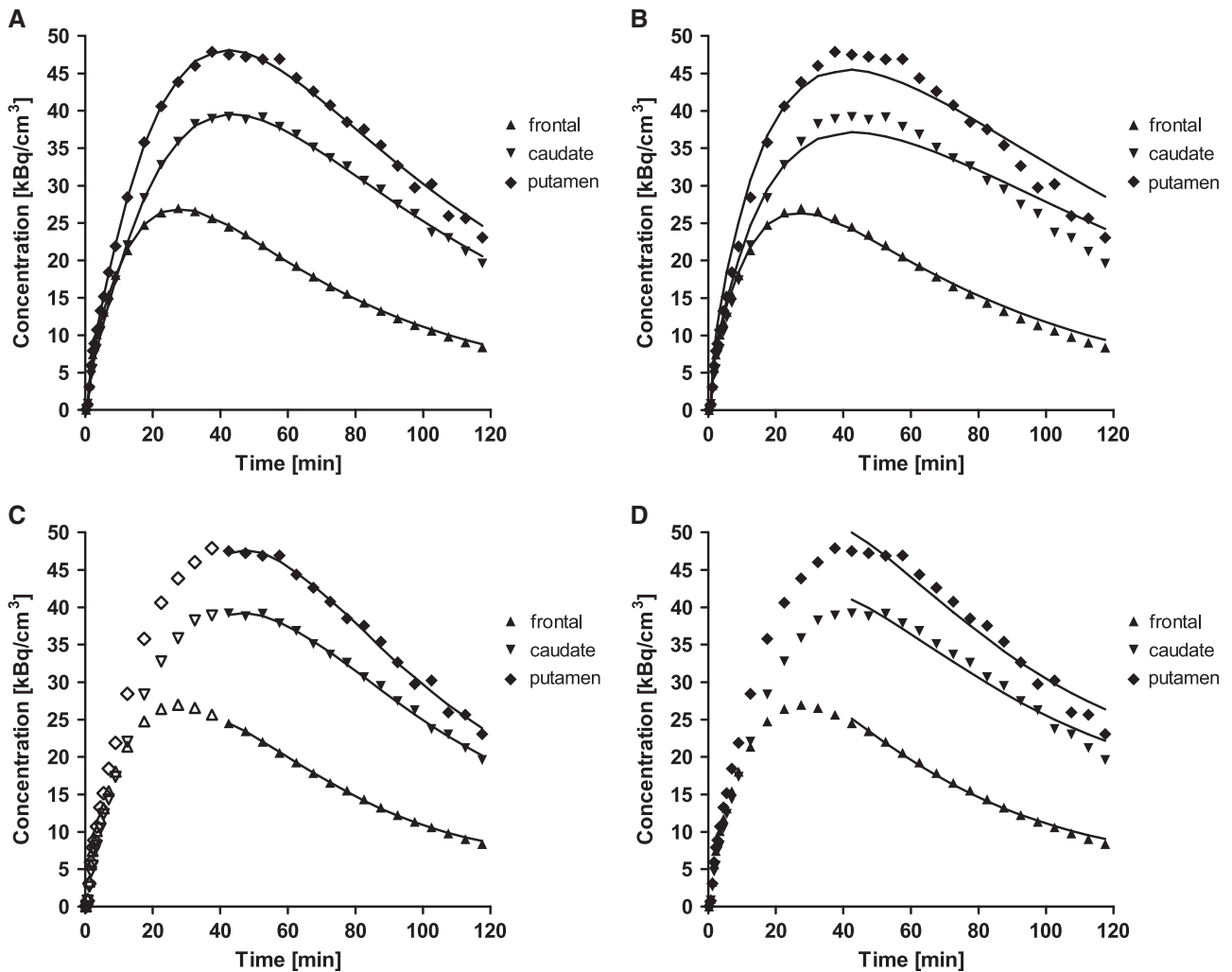
^aValues are means (%COV, intersubject variability) in 10 subjects. ^b t^* was set to 40 minutes after injection.

Figure 4. Typical examples of fitting methods based on a reference region (cerebellum) (A) simplified reference tissue model (SRTM), (B) SRTM2, (C) multilinear reference tissue model (MRTM), and (D) MRTM2. The values of k_2 in SRTM2 and MRTM2 were set to the population average. Points are concentrations measured in the frontal lobe (triangles, \blacktriangle), caudate (downward-pointing triangles, \blacktriangledown), and putamen (diamonds, \blacklozenge). The starting point for fitting, t^* , was set to 40 minutes for panels C and D; points used for the regression are shown in closed symbols.

well as good fits. Intersubject variability of BP_{ND} estimates was similar among MRTM, MRTM2, and MRTM2pop.

Parametric Imaging

Parametric images of BP_{ND} (MA1 and MRTM2) are shown in Figure 5. Highest binding was seen in the thalamus, striatum, and raphe regions. Given the smoothing parameters chosen, the parametric images had low noise, and the statistical quality of MA1 and MRTM2 images was similar. Region of interests were applied to the parametric images, and BP_{ND} values were compared with those from the MA1 ROI analysis.

For all smoothing levels and models, regional BP_{ND} values correlated well with those from MA1 ROI analysis. Because of the noise included in the unsmoothed image, the parametric V_T images using MA1 included some voxels with negative values or unreasonably high values (>50). In all models, regional BP_{ND} values decreased with larger FWHM (except for MRTM, between no smoothing and FWHM=3.6 mm). The value of b' (MRTM2) increased with larger FWHM, whereas the value of k'_2 (SRTM2) decreased ($b' = -23 \pm 2$ minutes, $k'_2 = 0.099 \pm 0.014/\text{min}$ at FWHM=3.6 mm). With a smoothing filter of 3.6 mm, the MA1 BP_{ND} estimates from parametric images matched well with those from ROI analysis ($BP_{ND}(\text{pix}, \text{MA1}) = 1.04 BP_{ND}(\text{ROI}, \text{MA1}) - 0.06$, $r^2 = 0.98$). The MRTM2 BP_{ND} estimates were also in excellent agreement with those from MA1 ($BP_{ND}(\text{pix}, \text{MRTM2}) = 0.99 BP_{ND}(\text{ROI}, \text{MA1}) + 0.04$, $r^2 = 0.98$). The comparison of the parametric and regional BP_{ND} values is shown in Figures 3C and 3D for MA1 and MRTM2, respectively, and in Supplementary Figure S5 for SRTM, SRTM2, and MRTM.

DISCUSSION

The primary aim of this study was to evaluate kinetic modeling methods and to determine the most appropriate method to obtain estimates of regional SERT densities with [¹¹C]AFM in the human brain. Because the 1T model did not adequately describe low-binding regions, the MA1 model was found to be quite appropriate for this tracer. The binding potential measure BP_{ND} was found to have the smallest intersubject coefficients of variation. Conventional reference tissue models (SRTM and MRTM) showed some underestimation of BP_{ND} , with best agreement to MA1 found for SRTM2 and MRTM2 with population k'_2 (or b').

Parent Fraction and Free Fraction in the Input Function

Like [¹¹C]DASB, metabolism of [¹¹C]AFM was rapid. For [¹¹C]DASB, an increase in parent fraction from 2 to 12 minutes after injection was reported by Parsey *et al.*³⁶ This pattern was absent for other SERT PET ligands in humans, such as [¹¹C]McN5652 and [¹¹C]MADAM. We did not observe this pattern in our study either. Comparing parent fractions at 3, 7, and 15 minutes in each subject, the fraction decreased monotonically in most cases. In one subject, the parent fraction at 7 minutes was higher than that at 3 minutes by 2%. The initial metabolism rate of [¹¹C]AFM was faster or similar to that of [¹¹C]DASB.^{28,35,37}

The effect of interpolation/extrapolation of parent fraction curves was investigated: (1) Assuming very slow metabolism at early time, i.e., the first 3 minutes parent fraction was set to one. (2) Avoiding the potential extrapolation errors, the parent fraction at 90 to 120 minutes was set to be the (constant) 90-minute value. Both cases are not physiologic, but they would be potentially large effects given the use of the exponential function. The V_T estimates using MA1 decreased by ~3% in both cases. These results indicate that interpolation/extrapolation errors effect is small.

We adopted the column-switching method of Hilton *et al.*¹⁸ for metabolite analysis. This method permits the use of larger volumes of plasma producing higher radioactivity levels and lower statistical noise in the final results compared with protein

precipitation method previously used in our lab. Application of this method was important because statistical errors in the low parent fraction values at later time points introduced variability into the fitting results.

All metabolites and radiochemical impurities were more polar than the parent compound, i.e., they eluted earlier in the analytical HPLC chromatogram. It is not known if the metabolites and/or impurities can enter the brain in humans, but in rat studies, HPLC analysis of rat brains showed that the parent compound accounted for $>95\%$ of the total radioactivity at 10 and 30 minutes after the injection, whereas at the same time points, the parent compound accounted for only 20% and 10% of the radioactivity in the plasma,⁸ respectively. These results in rat brain are suggestive that the metabolites and impurities do not enter the brain in humans.

The plasma free fraction of [¹¹C]McN5652 is not measurable. In contrast, [¹¹C]AFM plasma free fraction was low ($8.6 \pm 1.8\%$), but high enough to be measurable, and similar to that of [¹¹C]DASB ($8.9 \pm 1.6\%$).²⁸ The plasma free fraction for other SERT ligands, [¹¹C]MADAM and [¹¹C]HOMADAM, was not reported.

Compartmental Modeling and Graphical Analysis

Kinetic analyses indicated that both 1T and 2T compartment models were not sufficient to represent regional brain uptake curves for the following reasons. First, the 1T model showed lack of fit in intermediate and low-binding regions. The 1T fitted curves were above the actual activity levels at intermediate time points and below at late time points. Frankle *et al.*²⁸ reported a similar pattern in a study with [¹¹C]DASB. Second, the 2T model generated implausible parameter estimates in most cases, although it did converge in all cases. V_T is determined by the model prediction of the shape of the curves after the end of the scan as well as by the height of the tails of the curves. For a bolus injection, V_T is $\int_0^\infty C_T(t)dt / \int_0^\infty C_P(t)dt$.³⁸ In real situation, PET data are not acquired to infinity. The model provides an extrapolation of the PET data. In the 1T model, the extrapolation is performed by estimating only one exponential rate (k_2) and one scale factor (K_1). In the 2T model, there are two exponential rates and two scale factors, which cause the model-predicted extrapolation to become more unstable. There are many tracers for which the unconstrained 2T model does not provide stable V_T estimates, including [¹¹C]DASB.^{37,39} Fit quality, Akaike information criterion, and Schwartz criterion were not improved by the 2T model in SERT-rich regions. This is because of the greater difficulty in determining the 2T parameters in regions with a high fraction of specific binding as reflected in larger BP_{ND} .⁴⁰

The multilinear analysis MA1, which is based on the graphical analysis approach, constitutes a trade-off between the lower quality of fit of the 1T model and the greater instability of the 2T model. Similar types of lack of fit were observed with the 1T model or MA1 method with early t^* . When a later t^* setting was used, MA1 provided good fit quality in most regions, although some lack of fit could still be seen in the cerebellum and other low-binding regions, which were better fitted by the 2T model. Here, based on curve fitting and time stability of estimates, the MA1 model with later t^* was chosen as the method of choice for analysis. An early t^* results in poor quality of fit and bias in V_T estimate. Conversely, a late t^* results in greater variability in V_T estimates because too few points are available for the fitting. It is common to select the value of t^* based on visual inspection in a graphical analysis.^{41–44} The chosen t^* value (40 minutes) is a compromise to balance the quality of fit (and thus bias) and variability in V_T estimates. By setting t^* to 40 minutes, we minimize both the bias and instability in V_T estimates.

Different models have been proposed as appropriate for the analysis of [¹¹C]DASB data: the 1T model,²⁸ constrained 2T model,³⁷ and likelihood estimation in graphical analysis.⁴² For

[¹¹C]MADAM and [¹¹C]HOMADAM, the 2T model failed to provide stable rate constants.^{14,15} Appropriate models for [¹¹C]MADAM are constrained 2T model and Logan graphical analysis. For [¹¹C]HOMADAM, the 1T model was chosen. Here, based on curve fitting and time stability of estimates, the MA1 model with later t^* was chosen as the method of choice for analysis. However, model choice may evolve with the addition of data from more subjects.

From the correlation with the BP_{ND} estimates by MA1 model (Figure 3 and Supplementary Figure S5), SRTM, SRTM2, MRTM, and MRTM2 produced lower BP_{ND} estimates in high-binding regions. Because the 1T model does not fit well the [¹¹C]AFM data, the assumptions of SRTM and SRTM2 are violated. However, there are examples where SRTM can provide good quality fits for tracers whose TACs are not well fitted by the 1T model, e.g., [¹¹C]PHNO ([¹¹C](+)-4-propyl-3,4,4a,5,6,10b-hexahydro-2H-naphtho[1,2-b][1,4]oxazin-9-ol),⁴⁵ [¹¹C]PE2I (N-3-isodoprop-2E-ethyl)-2β-carbo[¹¹C]methoxy-3β-(4-methylphenyl)nortropane),⁴⁶ or [¹¹C]P943.⁴⁷ For such tracers, SRTM BP_{ND} estimates can match those obtained with arterial input function data (e.g., [¹¹C]PHNO), or be biased (e.g., [¹¹C]PE2I and [¹¹C]P943). [¹¹C]AFM belongs to the second category, where TACs are well fitted with SRTM, but SRTM BP_{ND} estimates are biased. Therefore, quality of fit can be deceptive for reference tissue models, and it is important to determine a gold standard model using an input function before reference tissue methods are investigated. The fits with SRTM2pop and MRTM2pop are visually not optimal. However, considering that MA1 V_T estimates matched well with 2T V_T estimates and that SRTM2pop and MRTM2pop provides comparable results to MA1, SRTM2pop and MRTM2pop are acceptable methods.

The value of kinetic parameter, K_1 , was moderate to high, indicating that [¹¹C]AFM is well extracted from the plasma. This K_1 was higher than that of [¹¹C]MADAM, similar to [¹¹C]DASB, and lower than that of [¹¹C]HOMADAM. Similar to [¹¹C]DASB and many other tracers, [¹¹C]AFM K_1 values are high compared with the theoretical maximum value, the cerebral blood flow, even though the plasma free fraction f_p is low (<10%). This combination of K_1 and f_p values can be explained if the [¹¹C]AFM–plasma protein association and dissociation rates are fast, and that within one capillary transit, all/most of the tracer in the plasma is effectively available for extraction into tissue.

Using fairly strict criteria, the minimal scan duration for [¹¹C]AFM was determined based on MA1 analysis ($t^* = 40$ minutes) and found to be 70 to 90 minutes. In raphe regions, the optimal minimal scan duration could not be determined. Raphe regions and amygdala have slow kinetics and thus require longer scanning time. Except for raphe, a 90-minute scan is sufficient for reliable estimates of [¹¹C]AFM binding parameters with MA1 analysis.

Among the three definitions of binding potential, BP_{ND} showed the smallest intersubject variability. Calculation of BP_P assumes that f_p is similar across subjects, and BP_{ND} assumes a similar f_{ND} across subjects. In this study, the intersubject variation in free fraction was similar between the plasma f_p (~20%) and the nondisplaceable compartment f_{ND} (~20%); however, f_{ND} is derived from f_p , so this agreement may not be surprising. This suggests that variability in the measurement of the input function is a substantial contributor to the larger intersubject variability in BP_P and BP_{ND} . Interestingly, [¹¹C]DASB showed the opposite results: BP_P displayed smaller intersubject variability (coefficients of variation) than BP_{ND} when the 1T model was used ($n = 6$).²⁸

Comparison of Various Serotonin Transporter Tracers

All the four diphenyl sulfide-derived SERT tracers ([¹¹C]DASB, [¹¹C]MADAM, [¹¹C]HOMADAM, and [¹¹C]AFM) show a high selectivity to SERT. Among the four tracers, [¹¹C]HOMADAM displays the fastest kinetics, with early regional peak uptake times of 10 to 40 minutes.¹⁵ Regional peak uptake times for [¹¹C]MADAM

range from 25 to 70 minutes.¹⁴ [¹¹C]DASB and [¹¹C]AFM have slightly slower uptake, with regional peak uptake times of 30 to 70 minutes.²⁸ Correspondingly, the minimal scanning time to estimate stable outcome measures is the shortest for [¹¹C]HOMADAM (65 minutes) and longer for [¹¹C]DASB and [¹¹C]AFM (90 minutes).

[¹¹C]AFM V_T and BP_{ND} values were compared with those of [¹¹C]DASB, [¹¹C]MADAM, and [¹¹C]HOMADAM. Note that the values for [¹¹C]DASB were variable in the literature. For this comparison purpose, values from Frankle *et al*³⁹ were used for [¹¹C]DASB. [¹¹C]AFM V_T and BP_{ND} values were highest among the four tracers across regions. Nonspecific binding, as measured by V_T in the cerebellum, is lowest for [¹¹C]HOMADAM, followed by [¹¹C]MADAM, and higher for [¹¹C]DASB and [¹¹C]AFM.

BP_{ND} is the most critical parameter to evaluate tracers, although other factors (e.g., peripheral metabolism rate) also play a role. [¹¹C]AFM BP_{ND} values in SERT-rich regions was 2.6, 2.1, and 1.6 times higher than those of [¹¹C]DASB, [¹¹C]MADAM, and [¹¹C]HOMADAM, respectively. In neocortical regions, [¹¹C]AFM BP_{ND} values were 6.7, 1.4, and 1.4 times higher than those of [¹¹C]DASB, [¹¹C]MADAM, and [¹¹C]HOMADAM, respectively. Note that these parameters were obtained from scanners with different spatial resolution (EXACT HR+ scanner for [¹¹C]DASB, EXACT HR47 scanner for [¹¹C]MADAM, and HRRT scanner for [¹¹C]HOMADAM). According to Schain *et al*,⁴⁸ SRTM BP_{ND} values for [¹¹C]MADAM were higher by ~20% on average with HRRT than the HR+.

Cerebellum as a Reference Region

According to previous postmortem studies using [³H]paroxetine binding,^{2-5,26} nondetectable or extremely low SERT density was detected in the cerebellum. However, several blocking studies showed that there were changes in radioligand binding in the cerebellum, especially in the white matter and vermis.^{35,49} In this study, white matter, vermis, and cerebellar subregions with confirmed blocking effect by citalopram were excluded from the cerebellum region used in our analysis.

To estimate the fraction of specific binding in the cerebellum, we used information from semiquantitative Western blotting study by Kish *et al*,²⁶ which showed that the relative density of SERT in the frontal lobe as compared with cerebellum was 5.3. The V_T values in the cerebellum and frontal lobe were 10.6 and 16.6 (mL/cm³), respectively, in our measurement (Table 1). Assuming that nonspecific binding is equal in both regions, 13% of the V_T in the cerebellum corresponds to specific binding (V_T in cerebellum = $V_{ND} + V_S = 10.6$, V_T in frontal lobe = $V_{ND} + 5.3V_S = 16.6$, $V_S = 1.40$). According to a similar estimate between other ROIs and cerebellum, the specific binding distribution volume V_S was 13 ± 6% of the V_T in the cerebellum, which would lead to a region-dependent underestimation of BP_{ND} : 13% in the amygdala, 15% in the hippocampus, 35% in the occipital lobe, and 42% in the frontal lobe. Thus, the effect of this bias must be carefully considered before using reference region analysis methods for [¹¹C]AFM, and potentially for other SERT tracers as well.

Quantification in the Raphe Nuclei

The raphe nuclei can be easily visualized in [¹¹C]AFM parametric images (Figure 5), especially with a high-resolution scanner. The high levels of SERT in the raphe nuclei lead to very high V_T values and extremely slow kinetics. When combined with the small size of the raphe regions and the short half-life of C-11, there is insufficient statistical quality in the late PET data to provide reliable estimates of V_T or BP_{ND} by any kinetic method. Compared to previous studies with [¹¹C]DASB, this effect is more pronounced because of the high resolution of the HRRT used in this study and the higher binding affinity of AFM relative to DASB. Note that it is not unusual for tracers to be suitable for proper quantification only in certain regions of the brain, with kinetics matched to their

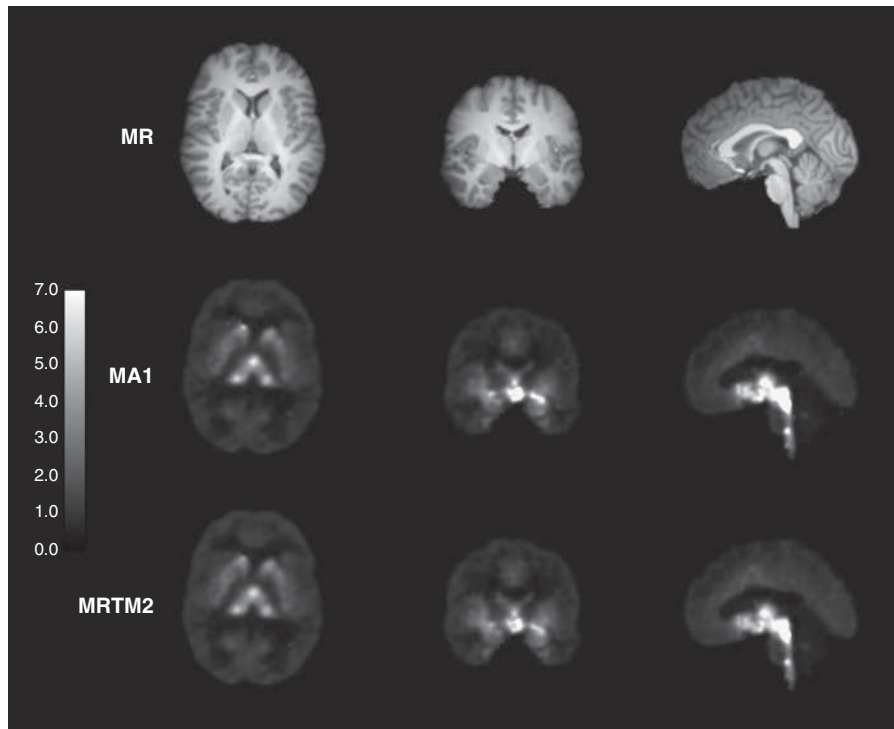


Figure 5. Typical coregistered magnetic resonance (MR) anatomic image (top) and parametric binding potential (BP_{ND}) images derived from multilinear analysis-1 (MA1) (middle) and two-parameter multilinear reference tissue model (MRTM2) (bottom). Images were generated with a pre-smoothing filter (three-dimensional Gaussian filter, full-width at half-maximum = 3.6 mm). The BP_{ND} color scale ranged from 0 to 7.

radioisotope half-lives, especially when the density of targeted receptor/transporter varies greatly across regions.

Binding Potential Parametric Imaging

In general, image smoothing and/or limits in the permitted range of k_2 values for the basis functions are required to calculate stable parametric images. The 1T, SRTM, and SRTM2 methods were implemented using a basis function method with specified range of k_2 values. We set a minimum k_2 value of 0.005/min; however, the k_2 value is <0.005 /min in some voxels in the SERT-rich regions. As a result, the estimated V_T or BP_{ND} values in such regions are somewhat biased. However, k_2 values are not limited in the multilinear methods MA1, MRTM, and MRTM2. To reduce the noise of image data, spatial smoothing or other noise reduction methods is recommended as a preprocessing procedure for these methods. As a result of image smoothing, spatial resolution is reduced and the voxel values in the small regions such as raphe and amygdala were biased by the partial volume effect. Although the starting time for MA1, MRTM, and MRTM2 was selected based on ROI analysis, it might not be early enough to obtain stable fitting in parametric imaging.

The MRTM2 method overestimated BP_{ND} values without image smoothing, although the value of b' was closest to that of MA1 ROI analysis. This bias was presumably caused by noise sensitivity of MRTM2. With a 3.6-mm image smoothing, the b' value changed substantially from that of MA1 ROI analysis. However, BP_{ND} values derived from parametric imaging with MRTM2 were close to those from MA1 ROI analysis. Thus, the two bias effects (difference in b' and noise) tend to cancel each other out.

[¹¹C]AFM can be used to visualize and quantify SERT binding in the human brain. Compared with previous SERT tracers, [¹¹C]AFM showed higher specific binding in areas with low SERT densities. The MA1 method is the most suitable kinetic analysis approach

with arterial input functions, both for ROI analysis and for parametric images. Among the reference region methods, MRTM2pop and SRTM2pop produced estimates comparable to those from MA1 ROI analysis and MRTM2 appears to be the most appropriate method for parametric imaging.

DISCLOSURE/CONFLICT OF INTEREST

The authors declare no conflict of interest.

REFERENCES

- 1 Lucki I. The spectrum of behaviors influenced by serotonin. *Biol Psychiatry* 1998; **44**: 151–162.
- 2 Cortés R, Soriano E, Pazos A, Probst A, Palacios JM. Autoradiography of antidepressant binding sites in the human brain: localization using [³H]imipramine and [³H]paroxetine. *Neuroscience* 1988; **27**: 473–496.
- 3 Laruelle M, Vanisberg MA, Maloteaux JM. Regional and subcellular localization in human brain of [³H]paroxetine binding, a marker of serotonin uptake sites. *Biol Psychiatry* 1988; **24**: 299–309.
- 4 Backström I, Bergström M, Marcusson J. High affinity [³H]paroxetine binding to serotonin uptake sites in human brain tissue. *Brain Res* 1989; **486**: 261–268.
- 5 Rosel P, Menchon JM, Oros M, Vallejo J, Cortadellas T, Arranz B *et al*. Regional distribution of specific high affinity binding sites for ³H-imipramine and ³H-paroxetine in human brain. *J Neural Transm* 1997; **104**: 89–96.
- 6 Suehiro M, Scheffel U, Ravert HT, Dannals RF, Wagner Jr. HN. [¹¹C](+)-McN5652 as a radiotracer for imaging serotonin uptake sites with PET. *Life Sci* 1993; **53**: 883–892.
- 7 Wilson AA, Ginovart N, Schmidt M, Meyer JH, Threlkeld PG, Houle S. Novel radiotracers for imaging the serotonin transporter by positron emission tomography: synthesis, radiosynthesis, and in vitro and ex vivo evaluation of ¹¹C-labeled 2-(phenylthio)araalkylamines. *J Med Chem* 2000; **43**: 3103–3110.
- 8 Huang Y, Hwang DR, Bae SA, Sudo Y, Guo N, Zhu Z *et al*. A new positron emission tomography imaging agent for the serotonin transporter: synthesis, pharmacological characterization, and kinetic analysis of [¹¹C]-2-[2-(dimethylaminomethyl)phenylthio]-5-fluoromethylphenylamine ([¹¹C]AFM). *Nucl Med Biol* 2004; **31**: 543–556.

- 9 Vercoullie J, Tarkiainen S, Halldin C, Emond P, Chalon S, Sandell J et al. Precursor synthesis and radiolabelling of [¹¹C]ADAM: a potential radioligand for the serotonin transporter exploration by PET. *J Labelled Comp Rad* 2001; **44**: 113–120.
- 10 Huang Y, Hwang DR, Zhu Z, Bae SA, Guo N, Sudo Y et al. Synthesis and pharmacological characterization of a new PET ligand for the serotonin transporter: [¹¹C]5-bromo-2-[2-(dimethylaminoethylphenylsulfanyl)]phenylamine ([¹¹C]DAPA). *Nucl Med Biol* 2002; **29**: 741–751.
- 11 Huang Y, Hwang DR, Narendran R, Sudo Y, Chatterjee R, Bae SA et al. Comparative evaluation in nonhuman primates of five PET radiotracers for imaging the serotonin transporters: [¹¹C]McN 5652, [¹¹C]ADAM, [¹¹C]DASB, [¹¹C]DAPA, and [¹¹C]AFM. *J Cereb Blood Flow Metab* 2002; **22**: 1377–1398.
- 12 Tarkiainen J, Vercoullie J, Emond P, Sandell J, Hiltunen J, Frangin Y et al. Carbon-11 labelling of MADAM in two different positions: a highly selective PET radioligand for the serotonin transporter. *J Labelled Comp Rad* 2001; **44**: 1013–1023.
- 13 Jarkas N, Votaw JR, Voll RJ, Williams L, Camp VM, Owens MJ et al. Carbon-11 HOMADAM: a novel PET radiotracer for imaging serotonin transporters. *Nucl Med Biol* 2005; **32**: 211–224.
- 14 Lundberg J, Odano I, Olsson H, Halldin C, Farde L. Quantification of ¹¹C-MADAM binding to the serotonin transporter in the human brain. *J Nucl Med* 2005; **46**: 1505–1515.
- 15 Nye JA, Votaw JR, Jarkas N, Purselle D, Camp V, Bremner JD et al. Compartmental modeling of ¹¹C-HOMADAM binding to the serotonin transporter in the healthy human brain. *J Nucl Med* 2008; **49**: 2018–2025.
- 16 Stockmeier CA. Involvement of serotonin in depression: evidence from postmortem and imaging studies of serotonin receptors and the serotonin transporter. *J Psychiatr Res* 2003; **37**: 357–373.
- 17 Carson RE, Barker WC, Liow JS, Johnson CA. Design of a motion-compensation OSEM list-mode algorithm for resolution-recovery reconstruction for the HRRT. *IEEE 2003 Nuclear Sci Symp Conf Rec* 2003; **5**: 3281–3285.
- 18 Hilton J, Yokoi F, Dannals RF, Ravert HT, Szabo Z, Wong DF. Column-switching HPLC for the analysis of plasma in PET imaging studies. *Nucl Med Biol* 2000; **27**: 627–630.
- 19 Tzourio-Mazoyer N, Landeau B, Papathanassiou D, Crivello F, Etard O, Delcroix N et al. Automated anatomical labeling of activations in SPM using a macroscopic anatomical parcellation of the MNI MRI single-subject brain. *NeuroImage* 2002; **15**: 273–289.
- 20 Holmes CJ, Hoge R, Collins L, Woods R, Toga AW, Evans AC. Enhancement of MR images using registration for signal averaging. *J Comput Assist Tomogr* 1998; **22**: 324–333.
- 21 Viola P, Wells III WM. Alignment by maximization of mutual information. *Int J Comput Vision* 1997; **24**: 137–154.
- 22 Ding YS, Singhal T, Planeta-Wilson B, Gallezot JD, Nabulsi N, Labaree D et al. PET imaging of the effects of age and cocaine on the norepinephrine transporter in the human brain using (S,S)-[¹¹C]O-methylreboxetine and HRRT. *Synapse* 2010; **64**: 30–38.
- 23 Huang Y, Neumeister A, Williams W, Ropchan J, Labaree D, Lin S et al. Comparative evaluation of the serotonin transporter tracers [C-11]AFM and [C-11]DASB in humans. *J Nucl Med* 2009; **50**: 1205 abstract.
- 24 Gunn RN, Gunn SR, Cunningham VJ. Positron emission tomography compartmental models. *J Cereb Blood Flow Metab* 2001; **21**: 635–652.
- 25 Innis RB, Cunningham VJ, Delforge J, Fujita M, Gjedde A, Gunn RN et al. Consensus nomenclature for in vivo imaging of reversibly binding radioligands. *J Cereb Blood Flow Metab* 2007; **27**: 1533–1539.
- 26 Kish SJ, Furukawa Y, Chang LJ, Tong J, Ginovart N, Wilson A et al. Regional distribution of serotonin transporter protein in postmortem human brain: is the cerebellum a SERT-free brain region? *Nucl Med Biol* 2005; **32**: 123–128.
- 27 Ichise M, Toyama H, Innis RB, Carson RE. Strategies to improve neuroreceptor parameter estimation by linear regression analysis. *J Cereb Blood Flow Metab* 2002; **22**: 1271–1281.
- 28 Frankle WG, Huang Y, Hwang DR, Talbot PS, Slifstein M, Van Heertum R et al. Comparative evaluation of serotonin transporter radioligands ¹¹C-DASB and ¹¹C-McN 5652 in healthy humans. *J Nucl Med* 2004; **45**: 682–694.
- 29 Lammertsma AA, Hume SP. Simplified reference tissue model for PET receptor studies. *NeuroImage* 1996; **4**: 153–158.
- 30 Wu Y, Carson RE. Noise reduction in the simplified reference tissue model for neuroreceptor functional imaging. *J Cereb Blood Flow Metab* 2002; **22**: 1440–1452.
- 31 Ichise M, Liow JS, Lu JQ, Takano A, Model K, Toyama H et al. Linearized reference tissue parametric imaging methods: application to [¹¹C]DASB positron emission tomography studies of the serotonin transporter in human brain. *J Cereb Blood Flow Metab* 2003; **23**: 1096–1112.
- 32 Buck A, Westera G, vonSchulthess GK, Burger C. Modeling alternatives for cerebral carbon-11-iomazenil kinetics. *J Nucl Med* 1996; **37**: 699–705.
- 33 Akaike H. New look at statistical-model identification. *IEEE Trans Autom Control* 1974; **Ac19**: 716–723.
- 34 Schwarz G. Estimating dimension of a model. *Ann Stat* 1978; **6**: 461–464.
- 35 Hinz R, Selvaraj S, Murthy NV, Bhagwagar Z, Taylor M, Cowen PJ et al. Effects of citalopram infusion on the serotonin transporter binding of [¹¹C]DASB in healthy controls. *J Cereb Blood Flow Metab* 2008; **28**: 1478–1490.
- 36 Parsey RV, Ojha A, Ogden RT, Erlandsson K, Kumar D, Landgrebe M et al. Metabolite considerations in the in vivo quantification of serotonin transporters using ¹¹C-DASB and PET in humans. *J Nucl Med* 2006; **47**: 1796–1802.
- 37 Ginovart N, Wilson AA, Meyer JH, Hussey D, Houle S. Positron emission tomography quantification of [¹¹C]-DASB binding to the human serotonin transporter: modeling strategies. *J Cereb Blood Flow Metab* 2001; **21**: 1342–1353.
- 38 Lassen NA. Neuroreceptor quantitation in vivo by the steady-state principle using constant infusion or bolus injection of radioactive tracers. *J Cereb Blood Flow Metab* 1992; **12**: 709–716.
- 39 Frankle WG, Slifstein M, Gunn RN, Huang Y, Hwang DR, Darr EA et al. Estimation of serotonin transporter parameters with ¹¹C-DASB in healthy humans: reproducibility and comparison of methods. *J Nucl Med* 2006; **47**: 815–826.
- 40 Carson RE, Kiesewetter DO, Jagoda E, Der MG, Herscovitch P, Eckelman WC. Muscarinic cholinergic receptor measurements with [¹⁸F]FP-TZTP: control and competition studies. *J Cereb Blood Flow Metab* 1998; **18**: 1130–1142.
- 41 Parsey RV, Ogden RT, Mann JJ. Determination of volume of distribution using likelihood estimation in graphical analysis: elimination of estimation bias. *J Cereb Blood Flow Metab* 2003; **23**: 1471–1478.
- 42 Ogden RT, Ojha A, Erlandsson K, Oquendo MA, Mann JJ, Parsey RV. In vivo quantification of serotonin transporters using [¹¹C]DASB and positron emission tomography in humans: modeling considerations. *J Cereb Blood Flow Metab* 2007; **27**: 205–217.
- 43 Elmenhorst D, Meyer PT, Matusch A, Winz OH, Zilles K, Bauer A. Test-retest stability of cerebral A1 adenosine receptor quantification using [¹⁸F]CJPPX and PET. *Eur J Nucl Med Mol Imag* 2007; **34**: 1061–1070.
- 44 Zanderigo F, Ogden RT, Bertoldo A, Cobelli C, Mann JJ, Parsey RV. Empirical Bayesian estimation in graphical analysis: a voxel-based approach for the determination of the volume of distribution in PET studies. *Nucl Med Biol* 2010; **37**: 443–451.
- 45 Ginovart N, Willeit M, Rusjan P, Graff A, Bloomfield PM, Houle S et al. Positron emission tomography quantification of [¹¹C]-(-)-PHNO binding in the human brain. *J Cereb Blood Flow Metab* 2007; **27**: 857–871.
- 46 Seki C, Ito H, Ichimiya T, Arakawa R, Ikoma Y, Shidahara M et al. Quantitative analysis of dopamine transporters in human brain using [¹¹C]PE2I and positron emission tomography: evaluation of reference tissue models. *Ann Nucl Med* 2010; **24**: 249–260.
- 47 Gallezot JD, Nabulsi N, Neumeister A, Planeta-Wilson B, Williams WA, Singhal T et al. Kinetic modeling of the serotonin 5-HT_{1B} receptor radioligand [¹¹C]P943 in humans. *J Cereb Blood Flow Metab* 2010; **30**: 196–210.
- 48 Schain M, Toth M, Cselenyi Z, Stenkrone P, Halldin C, Farde L et al. Quantification of serotonin transporter availability with [¹¹C]MADAM—a comparison between the ECAT HRRT and HR systems. *NeuroImage* 2012; **60**: 800–807.
- 49 Parsey RV, Kent JM, Oquendo MA, Richards MC, Pratap M, Cooper TB et al. Acute occupancy of brain serotonin transporter by sertraline as measured by [¹¹C]DASB and positron emission tomography. *Biol Psychiatry* 2006; **59**: 821–828.

Supplementary Information accompanies the paper on the Journal of Cerebral Blood Flow & Metabolism website (<http://www.nature.com/jcbfm>)